



ORIGINAL RESEARCH ARTICLE

The Influence of Residual Stress on Fatigue Crack Growth Rates in Stainless Steel Processed by Different Additive Manufacturing Methods

Christine M. Smudde, Christopher C. San Marchi, Michael R. Hill, and Jeffery C. Gibeling 

Submitted: 1 July 2023 / Revised: 23 March 2024 / Accepted: 31 March 2024

The properties and microstructure of Type 304L stainless steel produced by two additive manufacturing (AM) methods—directed energy deposition (DED) and powder bed fusion (PBF)—are evaluated and compared. Localized heating and steep temperature gradients of AM processes lead to significant residual stress and distinctive microstructures, which may be process-specific and influence mechanical behavior. Test data show that materials produced by DED and PDF have small differences in tensile strengths but clear differences in residual stress and microstructural features. Measured fatigue crack growth rates (FCGRs) for cracks propagating parallel to and perpendicular to the build directions differ between the two AM materials. To separate the influences of residual stress and microstructure, K-control test procedures with decreasing and constant stress intensity factor ranges are used to measure FCGRs in the near-threshold regime (crack growth rates $\leq 1 \times 10^{-8}$ m/cycle). Residual stress is quantified by the residual stress intensity factor, K_{res} , measured by the online crack compliance method. Correcting the FCGR data for differences in K_{res} brings results for specimens of the two AM materials into agreement with each other and with results for wrought specimens, when the latter are corrected for crack closure. Differences in microstructure and tensile strength have an insignificant influence on FCGRs in these tests.

Keywords additive manufacturing, directed energy deposition, fatigue crack growth, laser powder bed fusion, microstructure, residual stress

1. Introduction

Two major metal powder additive manufacturing (AM) processes, laser directed energy deposition (DED) and laser powder bed fusion (PBF), are layer by layer manufacturing techniques that involve melting and subsequent solidification of feedstock powders. Each method has its own distinct process parameters such as laser power and scan velocity that control unique thermal cycles with steep temperature gradients, high cooling rates, and cyclic reheating/remelting of previously

deposited layers (Ref 1, 2). In both AM processes, the complex thermal history results in significant residual stress and nonequilibrium microstructures (Ref 3), which are known to influence mechanical performance. Yet, a direct comparison of the microstructure, residual stress, and fatigue performance of different AM manufacturing methods has not been performed, representing one combination of factors impeding this technology from realizing its full potential in cyclic load bearing applications (Ref 4). A deeper understanding of these factors affecting the reliability of AM material fatigue crack growth performance is critical for the widespread adoption of the technology.

The objective of this study is to determine the separate roles of residual stress and microstructure on fatigue crack growth rate (FCGR) in Type 304L stainless steel produced via DED and PBF. The process-induced residual stress of the as-built DED and PBF materials are characterized through slitting measurements and compared. The present experiments are used to evaluate FCGRs in the near-threshold regime ($da/dN \leq 10^{-8}$ m/cycle) and their extension into the Paris regime ($\Delta K \leq 10$ MPa $m^{0.5}$), but well below fracture (which is $K > 100$ MPa $m^{0.5}$) for crack growth both perpendicular and parallel to the build directions. The influence of process-induced residual stress on fatigue crack growth behavior is then quantified by the residual stress intensity factor, K_{res} , determined via the online crack compliance method (Ref 5-9). Values of K_{res} are used to correct measured fatigue crack growth data for the influence of residual stress (Ref 5, 6, 8) to enable an unbiased evaluation of other influences on FCGR, such as those arising from differences in orientation, microstructure and tensile strength.

This invited article is part of a special topical issue of the *Journal of Materials Engineering and Performance* on Residual Stress Analysis: Measurement, Effects, and Control. The issue was organized by Rajan Bhambroo, Tenneco, Inc.; Lesley Frame, University of Connecticut; Andrew Payzant, Oak Ridge National Laboratory; and James Pineault, Proto Manufacturing on behalf of the ASM Residual Stress Technical Committee.

Christine M. Smudde and **Jeffery C. Gibeling**, Department of Materials Science and Engineering, University of California, One Shields Avenue, Davis, CA 95616; **Christopher C. San Marchi**, Sandia National Laboratories, Livermore, CA 94550; and **Michael R. Hill**, Department of Mechanical and Aerospace Engineering, University of California, One Shields Avenue, Davis, CA 95616. Contact e-mail: jcgibeling@ucdavis.edu.

2. Material and Methods

2.1 Additively Manufactured Builds

Type 304L stainless steel material built via DED and PBF was evaluated in this study. Previously, the materials produced by both methods have been investigated individually (Ref 10, 11), but the influence of residual stress on their fatigue crack growth properties has not been directly compared. The chemical composition of gas atomized feedstock powders conformed to ASTM requirements for austenitic Type 304L stainless steel material (Ref 12) and has been reported elsewhere for DED and PBF (Ref 10, 11). Small differences in chemical composition were not expected to significantly influence fatigue performance; hence, this study is based on the expectation that the processing method is the primary difference between the two materials under consideration.

Two replicate DED builds (DED2 and DED3) were fabricated as vertical walls with nominal dimensions of 110 mm (*Z*-direction, build direction) × 56 mm (*Y*-direction) × 7.6 mm (*X*-direction). Both DED builds were produced on the same machine with the same processing parameters over the course of several weeks, which were optimized for 99.9% density and are described in an earlier study of the same material (Ref 13). Two nominally identical PBF builds (PBF-L1 and PBF-L2) were fabricated one year apart on the same machine. The PBF builds were deposited as vertical D-shaped cylinders with processing parameters described in previous work (Ref 11). Nominal dimensions of the wall of interest were 110 mm (*Z*-direction, build direction) × 36 mm (*Y*-direction) × 5.1 mm (*X*-direction). One build from each processing method was used to evaluate FCGRs with a crack propagating parallel to the build direction (vertical, *Y-Z*) and one build from each method was used to assess FCGRs with a crack propagating perpendicular to the build direction (horizontal, *Z-Y*). Three crack growth specimens were machined from each of the four builds.

2.2 Microstructure Evaluation

Microstructural heterogeneity was evaluated through electron backscatter diffraction (EBSD) imaging of the DED and PBF materials. Samples for material characterization were extracted via wire electrical discharge machining (EDM), mounted in epoxy and ground to 1200 grit prior to polishing with an alumina suspension of 3 mm, 1 mm, and 0.3 mm. Samples were then vibropolished for 8-9 hours with 0.05 mm colloidal silica prior to examination in the SEM. A Scios Dual-Beam FIB/SEM operating at 15 kV with 3 μm step size was used to examine differences in grain sizes and shapes in the DED and PBF materials in *X-Y* and *X-Z* planes. In addition, secondary electron (SE) imaging on a ThermoFisher Quattro ESEM operating at 5 kV and 0.11 nA was used to examine fatigue surfaces and backscatter electron (BSE) imaging at 5 kV and 0.46 nA to examine crack profiles.

2.3 Tensile Testing

Cylindrical specimens for conventional tensile testing were extracted from one replicate DED build and one replicate PBF build. The gauge length of the specimens was 19 mm and the diameter was 2.9 mm. An extensometer with a gauge length of 12.7 mm was used to determine strain during constant cross-head displacement testing at a rate of approximately 0.02 mm/

s. The 0.2% offset yield strength, ultimate tensile strength, elongation at failure and reduction of area are reported.

2.4 Residual Stress Measurement

Process-induced residual stress was evaluated in the DED and PBF builds. Plates from each build with similar dimensions in *Y* and *Z* were removed via wire EDM as shown by the thin vertical blue lines in Fig. 1. Vishay strain gages were applied on the EDM surface at two equally spaced locations (1 and 2). Build direction residual stress as a function of cut depth was then determined by the slitting method on the two planes of interest (horizontal black lines) (Ref 14). This method is a one-dimensional mechanical relaxation technique that uses strain measured at fixed cut increments (starting from the front face) to determine a through thickness (*X*-direction) average of residual stress acting in the build direction (*Z*-direction) as a function of distance from the front face (along the *Y*-direction). Detailed descriptions of this method are presented elsewhere (Ref 15, 16). Additional slitting measurements were performed during the machining of notches in fatigue crack growth rate test specimens as indicated by the red lines in Fig. 1(c).

To evaluate the contribution of residual stress to the stress intensity factor, values of K_{res} due to residual stress acting normal to the cut plane were determined from the strain data collected during slitting measurements. The derivative of the strain with respect to cut depth (or crack size), $d\varepsilon/da$, was found using a polynomial regression as described in previous work (Ref 10, 11, 17, 18). The strain derivative and a geometry dependent influence function ($Z(a)$) as described by Schindler (Ref 19) were then used to determine K_{res} as a function of crack size:

$$K_{res}(a) = \frac{E'}{Z(a)} \frac{d\varepsilon(a)}{da} \quad (\text{Eq 1})$$

where E' is the generalized elastic modulus, taken here as a handbook value of 200 GPa for Type 304L stainless steel under plane stress conditions (Ref 20).

The residual stress intensity factor was also determined in the fatigue test specimens by applying the online crack compliance (OLCC) method to the FCGR test data (Ref 5, 8, 9, 17). In this method, the residual strain (ε_{res}) is quantified by extrapolating the linear region of the load versus deformation data (i.e., compliance data) to zero load. The value of ε_{res} is nominally equivalent to the strain determined by a slitting measurement and can be used to determine K_{res} in the same way (Eq 1). Further details on the methodology for determining K_{res} during FCGR tests are available in recent work (Ref 17).

2.5 Fatigue Crack Growth Rate Testing

The DED and PBF plates were machined into compact (C(T)) specimens in accordance with ASTM E647 (Ref 18) having a specimen width (*W*) of 26.4 mm and thicknesses of 6.35 mm (DED) and 4.06 mm (PBF). Three specimens were extracted from each build for crack growth testing (Fig. 1). Specimens from the top and bottom (T and B) were used to evaluate near-threshold crack growth rates with decreasing applied stress intensity factor range tests (decreasing ΔK_{app}) (Ref 18); specimens from the middle (M) were tested under constant ΔK_{app} . Consistent with specimen designations of previous work (Ref 10, 11), FCGRs for a crack propagating perpendicular to the build direction (horizontal (H) crack

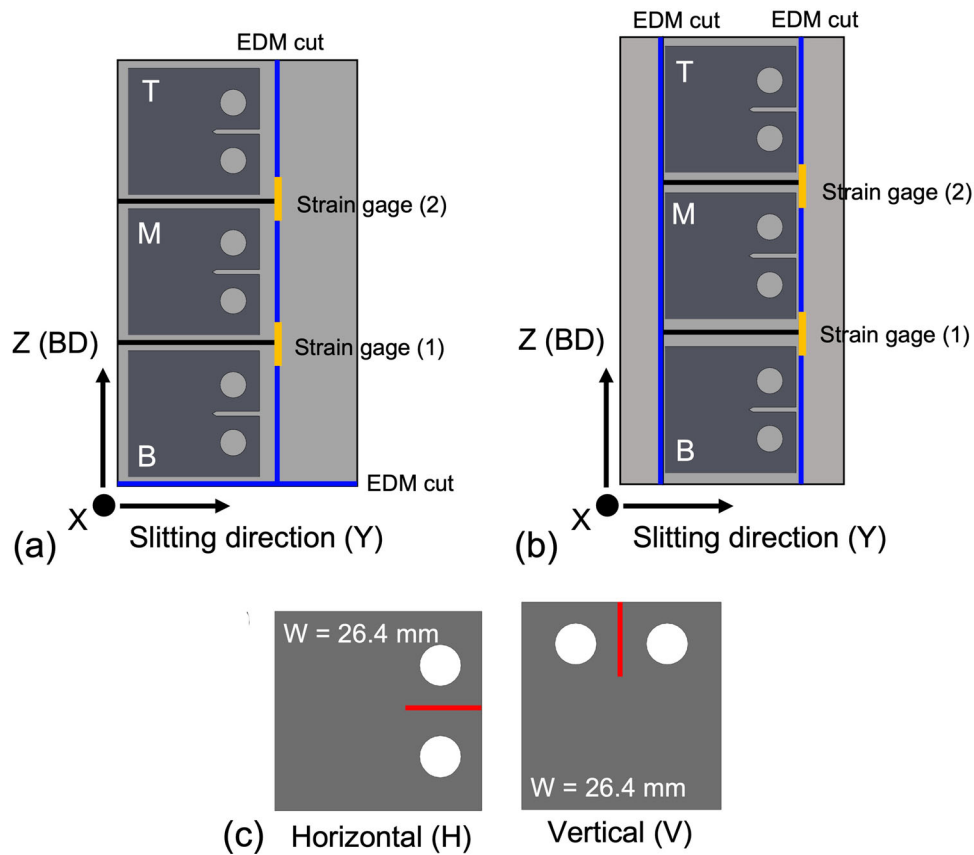


Fig. 1 Schematic of slitting measurements and specimen extraction of (a) DED and (b) PBF material with (c) C(T) specimen geometry and orientations (Color figure online)

Table 1 Specimen designations for K_{res} and FCGR measurements

Specimen	Specimen	Specimen	Specimen	FCGR test condition
DED2-B (H)	DED3-B (V)	PBF-L1-B (H)	PBF-L2-B (V)	Decreasing ΔK_{app}
DED2-M (H)	DED3-M (V)	PBF-L1-M (H)	PBF-L2-M (V)	Constant ΔK_{app}
DED2-T (H)	DED3-T (V)	PBF-L1-T (H)	PBF-L2-T (V)	Decreasing ΔK_{app}

growth) were determined from specimens extracted from DED2 and PBF-L1; whereas, FCGRs for a crack propagating parallel to the build direction (vertical (V) crack growth) were determined from specimens extracted from builds DED3 and PBF-L2. For reference, the specimen designations and the associated test conditions are presented in Table 1. Two C(T) specimens of each thickness, 6.35 mm and 4.06 mm, were cut from dual-certified, annealed, wrought Type 304/304L stainless steel and were tested under decreasing ΔK_{app} conditions to provide reference comparisons for the DED and PBF specimens at their respective thicknesses. Wrought 304L was chosen as the baseline for comparison because it represents the material that would most likely be replaced by additively manufactured 304L and therefore represents an appropriate standard for comparison.

An Instron 1331 servo-hydraulic load frame was utilized for fatigue testing in lab air at an applied stress ratio (R_{app}) of 0.1 and frequency of 10 Hz. All specimens (AM and wrought) were notched via wire EDM and fatigue precracked to a crack size (a) of 6.6 mm ($a/W = 0.25$) using the K-decreasing test

procedure (tension–tension, $R > 0$) in accordance with ASTM E647 (Ref 18). Vishay strain gages at the back face of each fatigue specimen were used to monitor back face strain (BFS) (Ref 10, 11). The MTS 790.40 fatigue crack growth software running on a MTS TestStar control system was modified to accept this BFS input to determine compliance and crack size (Ref 13). Constant ΔK_{app} fatigue tests were performed at ΔK_{app} of $6.6 \text{ MPa m}^{0.5}$ by using a load shedding parameter of $C = 0$ and decreasing ΔK_{app} fatigue tests had an initial K_{max} of $11.6 \text{ MPa m}^{0.5}$ and $C = -0.08 \text{ mm}^{-1}$ (Ref 18). During the fatigue crack growth tests, load and BFS data (i.e., compliance data) were recorded at crack size increments of 0.05 mm, each with 500 data points averaged over 3 consecutive cycles. Compliance data were then used for post-test data analysis of crack size, FCGRs and K_{res} via the online crack compliance (OLCC) method based on Eq 1. Post-test examination of fracture surfaces (described in (Ref 11, 13)) demonstrated that the crack sizes determined using specimen compliance and a modulus of 200 GPa agreed well with the physically measured crack sizes for both DED and PBF specimens. Thus, no

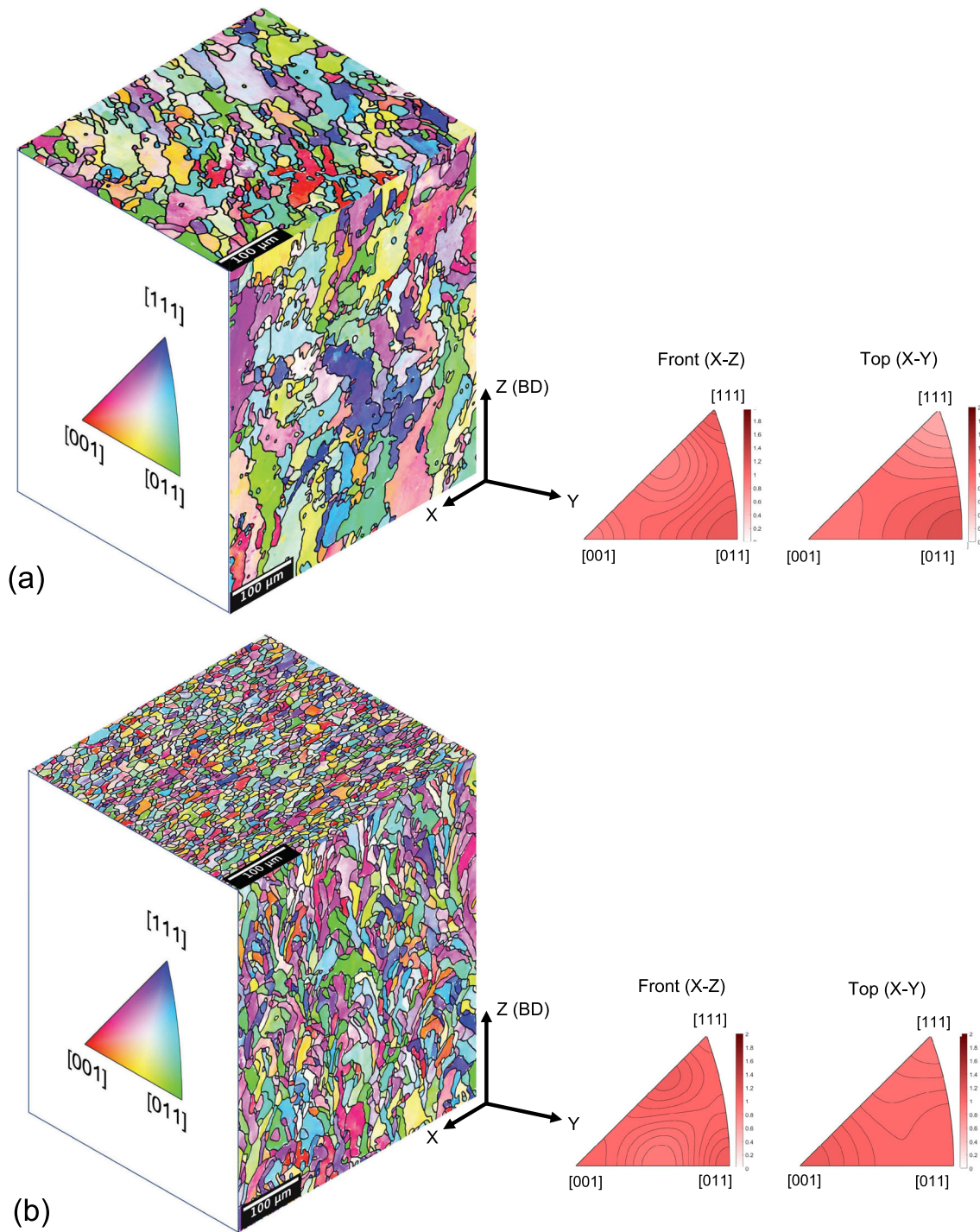
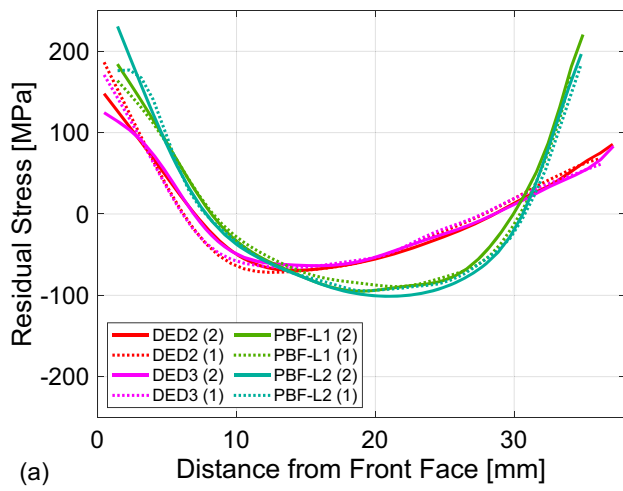


Fig. 2 EBSD orientation images for (a) DED material and (b) PBF material with IPF contour plots

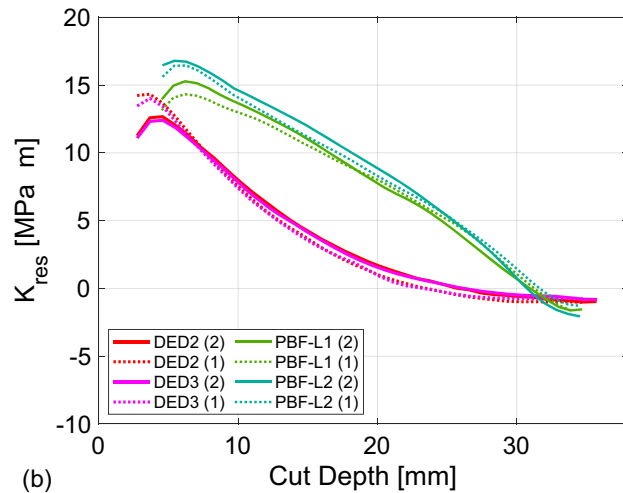
Table 2 Tensile properties of AM 304L, comparing PBF in the two principal orientations and DED (L orientation only)

Material designation	Orientation	Yield strength, MPa	Tensile strength, MPa	Elongation at failure, %	Reduction of area, %	Number of tests
DED	L	323 ± 5	621 ± 3	71 ± 2	79 ± 1	2
PBF	L	440 ± 10	648 ± 1	68 ± 2	83 ± 1	8
PBF	T	500 ± 2	698 ± 1	57 ± 1	84 ± 1	3

Range represents standard deviation.



(a) Residual Stress [MPa] vs. Distance from Front Face [mm]



(b) K_{res} [MPa√m] vs. Cut Depth [mm]

Fig. 3 (a) Residual Stress (RS) and (b) K_{res} profiles from slitting of DED and PBF plates

adjustment of the elastic modulus was needed to correct the compliance-derived crack sizes as specified in ASTM E647 (Ref 18). To account for the separate effects of residual stress and crack closure, values of K_{res} from each specimen were combined with independent calculations using the adjusted compliance ratio (ACR) method that accounts for crack closure effects ($\Delta K_{eff} = \Delta K_{ACR}$) (Ref 18, 21), resulting in a corrected stress intensity factor range (ΔK_{corr}) for all FCGR test data that was used to isolate intrinsic material performance (Eq 2) (Ref 5, 6, 8).

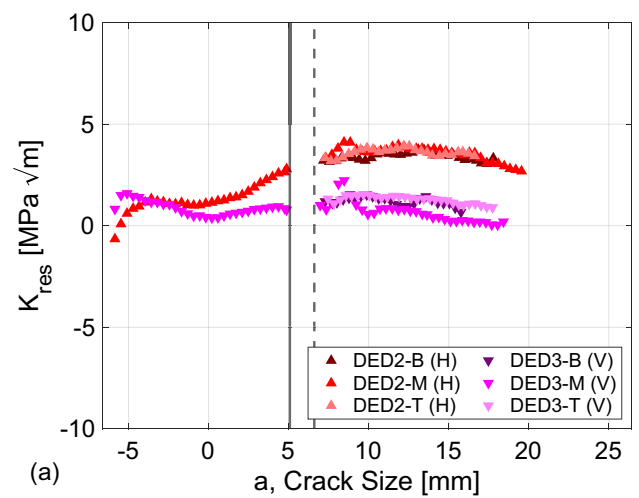
$$\Delta K_{corr}(a) = \Delta K_{eff}(a)^{1-n} (K_{max,app}(a) + K_{res}(a))^n (1 - R_{app})^n \quad (\text{Eq 2})$$

where $n = 0.25$ as determined previously (Ref 13).

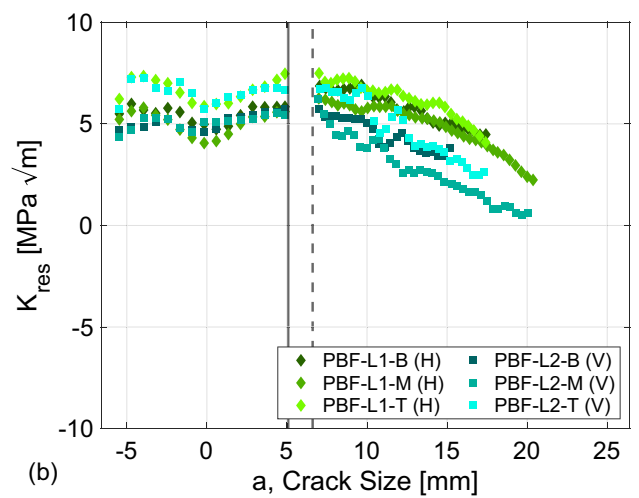
3. Results and Discussion

3.1 Microstructure

EBSD images and Inverse Pole Figure (IPF) contour plots for two unique microstructural planes (X - Y and Y - Z) are shown in Fig. 2(a) and (b) for the DED and PBF materials,



(a) Full K_{res} profile for DED C(T) fatigue specimens



(b) Full K_{res} profile for PBF C(T) fatigue specimens

Fig. 4 Full K_{res} profile for (a) DED and (b) PBF C(T) fatigue specimens with notch slitting to the left of the solid line and OLCC to the right of the dashed line (end of precrack)

respectively. Both exhibit similar grain shapes with a distinct elongation of grains in the build direction. Thus, the effective grain sizes are larger in the build direction than in the transverse direction. In the near-threshold regime, preferential grain orientations (crystallographic texture) may influence fatigue crack growth rates as cracks propagate in certain crystallographic directions. The relative lack of texture evident in the IPF contour plots for DED and PBF showing uniform coloration and small values suggests that it is not an important factor in this study.

The determination of crack size and K_{res} (Eq 1) both depend on elastic modulus as a material property. In a recent study, Charmi et al. (Ref 22) observed elastic anisotropy in PBF 316L wall builds up to $\pm 10\%$ for dynamic modulus measurements in the build direction and transverse to it. Therefore, it is important to consider whether elastic anisotropy might influence the present measurements. The tensile tests for this study were not conducted with sufficient extensometer resolution at small strains to determine accurate values of modulus; hence, other evidence must be used.

Two important factors that might influence the elastic modulus of AM materials are porosity and preferred orientations of grains. Charmi, et al. demonstrated that the variations

in elastic modulus with specimen orientation within wall builds were entirely explained by the crystallographic texture present in the builds that had limited porosity (Ref 22). The IPF contour plots shown in Fig. 2 reveal that there is no significant texture in the DED or PBF builds examined in this study. Furthermore, all builds were optimized for density and contained only minimal pores; hence, they have negligible porosity. Thus,

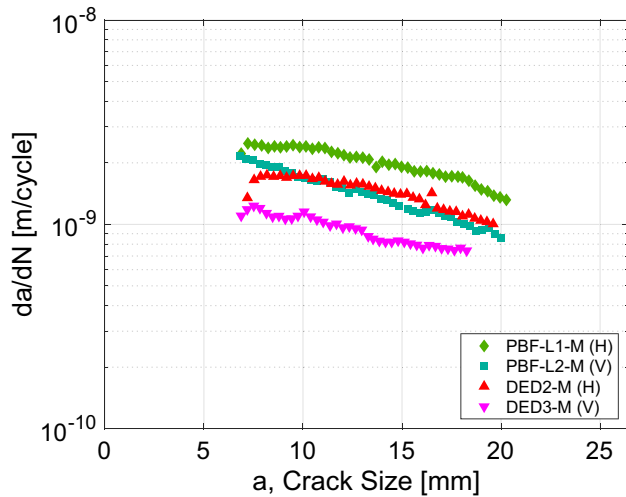


Fig. 5 Measured FCGRs for DED and PBF in constant ΔK_{app} tests

microstructural evidence indicates that there is no elastic anisotropy in these builds. Furthermore, as described earlier, the physically measured crack sizes agreed with those derived from compliance data obtained during the fatigue crack growth tests, demonstrating that the single modulus value of 200 GPa adequately characterizes the elastic properties of both builds.

The grain morphology of the DED material exhibits a large distribution of shapes and sizes, but with an average grain size that is larger than that of the PBF material. The DED process generally results in thicker layers with average cooling rates ranging from 100 to 10000 K/s (Ref 23-26). In contrast, the PBF process typically has a smaller layer thickness with significantly higher cooling rates of 10^6 to 40×10^6 K/s (Ref 27). As such, smaller solidification layers and faster cooling rates in the PBF process limit grain growth as compared to DED. The resulting finer microstructure of the PBF material would commonly be thought to benefit fatigue initiation resistance as characterized by the lifetime of cyclically loaded, smooth-sided specimens (Ref 28). In contrast, the coarser grains observed in DED material are expected to benefit fatigue crack growth resistance (Ref 29, 30).

3.2 Tensile Properties

The averages and standard deviations of the tensile properties are provided in Table 2 for all tested PBF longitudinal and transverse tensile specimens, along with the longitudinal tensile data from the tested DED specimens. Whereas the longitudinal tensile properties of the PBF materials are uniform

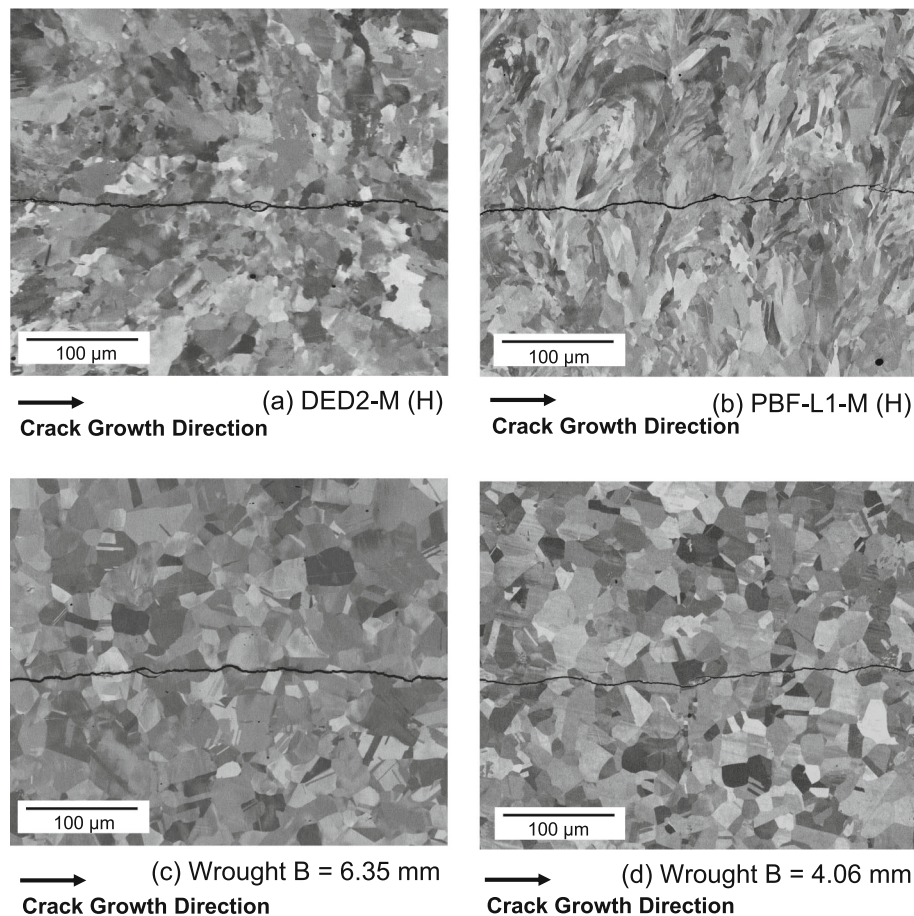


Fig. 6 Crack profile images of (a) DED2-M (H) (b) PBF-L1-M (H) (c) wrought ($B = 6.35$ mm) and (d) wrought ($B = 4.06$ mm)

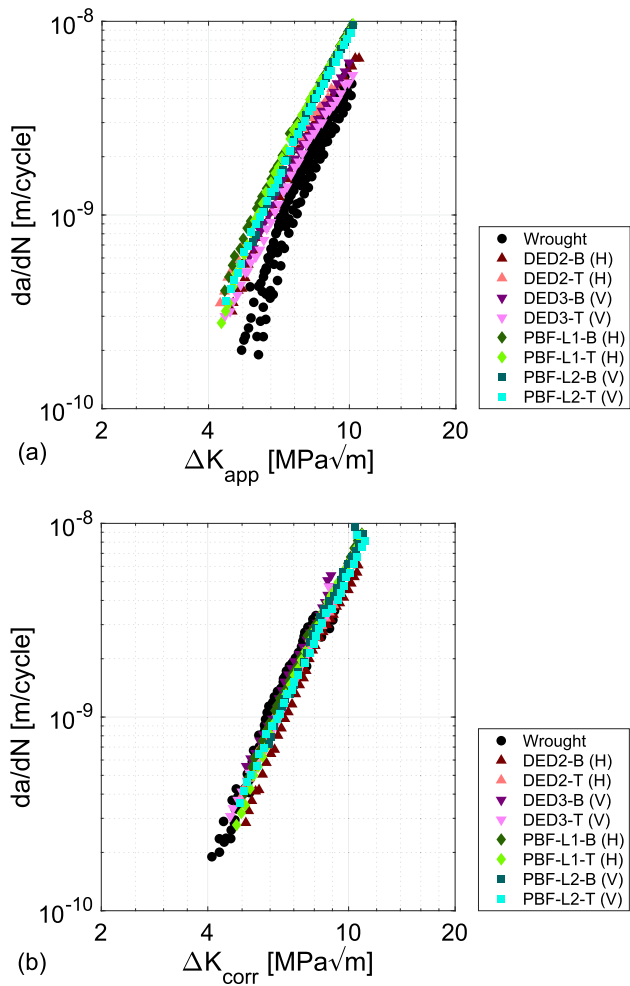


Fig. 7 (a) Measured FCGRs for DED and PBF compared to wrought and (b) corrected

across all specimens, the strength in the transverse direction is significantly greater than the longitudinal strength, consistent with the finer effective grain size in the former than in the latter. The DED material has a lower strength (with similar ductility), again consistent with its coarser grain size.

3.3 Residual Stress Results

Results from the initial slitting measurements made prior to FCGR specimen extraction are shown in Fig. 3. The overall residual stress profiles of both AM materials show a steep gradient of stress between the center (compression) and the edges of the plates (tension). The tensile residual stress at the edges contributes to positive K_{res} throughout most of the cut depth. Residual stress and K_{res} results from the four slitting measurements of the DED plates (two measurements from each of the two plates) demonstrate excellent agreement and indicate repeatability of the measurement as well as reproducibility between builds. The four results of the PBF plates also agree well, indicating that the build direction residual stress is

reproducible in the two PBF builds independent of when the deposition was made. The asymmetry in the residual stress profiles of the DED material is attributed to the off-center extraction of the DED plates (vertical blue lines in Fig. 1). The greater residual stress in PBF material, both tensile at the edges and compressive at the center, is attributed to the steeper temperature gradients, which are characteristic of the PBF process (Ref 1).

Figure 4(a) and (b) present the K_{res} results from notch slitting and OLCC for the DED and PBF specimens, respectively, with K_{res} in the specimens being smaller than those in the plates (which is consistent with stress release occurring during specimen extraction). The DED specimens have significant tensile K_{res} in the H orientation (3 to 4 MPa $m^{0.5}$ for all crack sizes) and smaller K_{res} in the V orientation (0-2 MPa $m^{0.5}$ for all crack sizes). The difference in K_{res} between orientations reflects larger residual stress in the build (Z) direction and smaller residual stress in the transverse (Y) direction. The PBF specimens have larger values of K_{res} as compared to DED for both orientations (H and V), being 5-7 MPa $m^{0.5}$ at the notch. Furthermore, K_{res} decreases more quickly with crack size than in the DED specimens, with values in H specimens dropping to 3 MPa $m^{0.5}$ at the longest crack size and V specimens to 1 MPa $m^{0.5}$. While there is a small difference in K_{res} with orientation for PBF specimens, there is a large difference with orientation for DED specimens, with much lower values in the DED (V) than in the PBF (V).

3.4 Fatigue Crack Growth

Crack growth rates from the constant ΔK_{app} fatigue tests are shown in Fig. 5. The trends in FCGRs of the DED and PBF specimens follow the trends in the K_{res} results shown in Fig. 4(a) and (b), respectively. Under constant ΔK_{app} , FCGRs decrease with increasing crack size, consistent with the decrease in positive K_{res} that results from the redistribution of tensile residual stress as the crack extends through the specimen. The PBF (H) specimen has the highest positive K_{res} for all crack sizes, which contributes to this specimen exhibiting the highest FCGRs. PBF (V) and DED (H) have similar values of K_{res} , and the similar FCGRs in these specimens are consistent with this measurement. DED (V) has the smallest positive values of K_{res} , and the lowest FCGR. Because K_{res} adds to both the minimum ($K_{min,app}$) and maximum ($K_{max,app}$) values of K_{app} , positive K_{res} increases the total stress intensity factor ratio, R_{tot} (where $R_{tot} = (K_{min,app} + K_{res}) / (K_{max,app} + K_{res})$) compared to the applied stress intensity factor ratio ($R_{app} = K_{min,app} / K_{max,app}$). Another way of describing this effect is that a positive K_{res} has the effect of increasing the mean value of K and the FCGRs. Fatigue crack growth data under constant ΔK_{app} for these AM materials and orientations are therefore typical of data in other metallic materials that show clear correlation between elevated R_{tot} and elevated FCGRs in the near-threshold regime (Ref 31). Additionally, both DED and PBF specimens demonstrated transgranular fatigue crack growth as shown in Fig. 6 and in previous work (Ref 10, 11) despite differences in grain size as

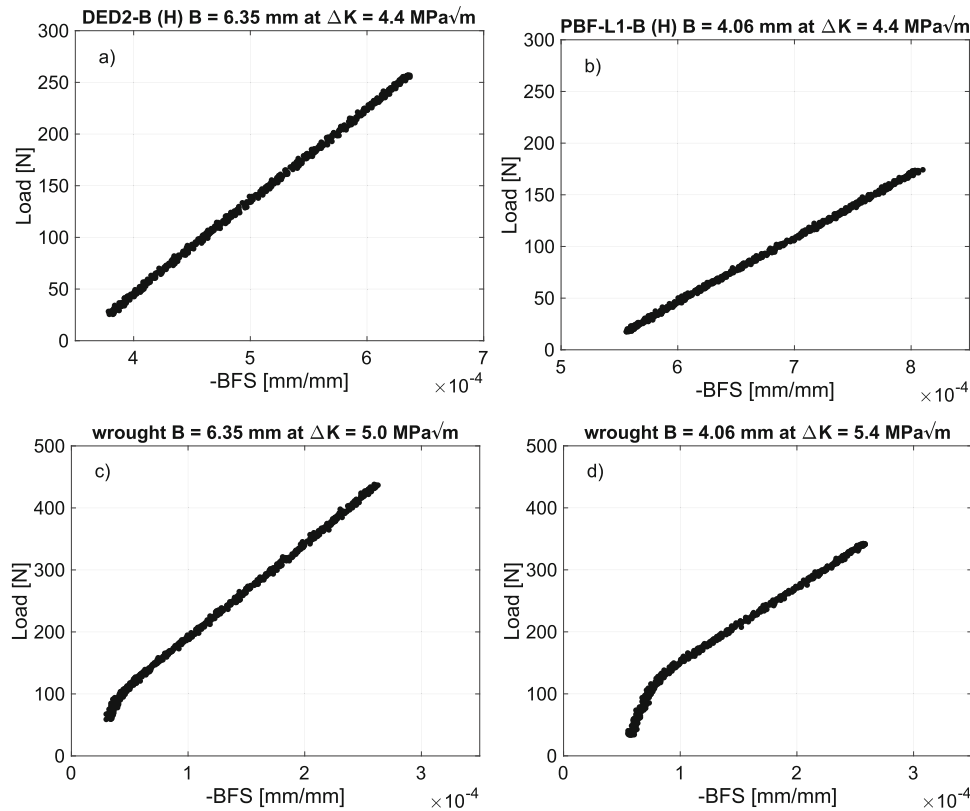


Fig. 8 Compliance plots for crack growth in the near-threshold region for (a) DED2-B (H) (b) PBF-L1-B (H) (c) wrought ($B = 6.35$ mm) (d) wrought ($B = 4.06$ mm) showing linearity in the presence of tensile residual stress (a) and (b) and deviations from linearity from crack closure (c) and (d)

shown in Fig. 2(a) and (b). This similarity of crack profiles suggests that residual stress has a more significant influence on FCGRs in specimens of these AM materials than does microstructure.

The measured FCGRs for the decreasing ΔK_{app} tests are presented in Fig. 7(a) for the AM and wrought specimens. At high values of ΔK_{app} near the beginning of the tests, there are clear differences in rate with the PBF specimens having the highest FCGRs followed by DED, and then wrought. These trends persist over several millimeters of crack growth and are consistent with the values of K_{res} in the specimens, where prior work (Ref 10, 11) showed wrought specimens to have negligible K_{res} . Consistent with the trends in Fig. 4(a) and (b) where K_{res} for both DED and PBF gradually converge to similar values in each orientation at crack sizes approaching 20 mm ($\sim 2.5 \text{ MPa}\cdot\text{m}^{0.5}$ in (H) and $\sim 0.5 \text{ MPa}\cdot\text{m}^{0.5}$ in (V)), the FCGRs for all AM specimens converge to a nominally common value ΔK_{app} between 4 and 5 $\text{MPa}\cdot\text{m}^{0.5}$ at the largest crack sizes in the threshold regime. The somewhat larger spread in FCGR for DED versus PBF, at ΔK_{app} between 7 and 10 $\text{MPa}\cdot\text{m}^{0.5}$, is consistent with the greater orientation differences in K_{res} for specimens of DED material. Both DED and PBF specimens have higher FCGRs at all values of ΔK_{app} compared to those of annealed wrought material.

While some differences in FCGR are due to the influence of residual stress, the rates for the wrought specimens are also affected by crack closure. Fig. 8 illustrates compliance data for representative loading cycles for wrought specimens (wrought ($B = 6.35$ mm) and wrought ($B = 4.06$ mm)) compared to PBF and DED specimens (DED2-B (H) and PBF-L1-B (H)). In

accord with the concepts introduced by Elber (Ref 32), the nonlinearity in the compliance data for the wrought condition indicates that crack closure reduces the effective driving force for fatigue crack growth in those specimens. The linearity of compliance data for the AM specimens suggests a lack of crack closure in those tests. In addition, the amount of crack closure is greater in the thinner wrought specimen ($B = 4.06$ mm) used for comparison to the PBF material, leading to lower FCGRs compared to the thicker specimen ($B = 6.35$ mm) used for comparison to the DED material.

To compare FCGR trends among the various specimens, ΔK was adjusted for the effects of residual stress and crack closure. As described in previous work (Ref 11), the influence of crack closure on ΔK was accounted for using the ACR method outlined in the appendix of ASTM E647 (Ref 18, 21). Subsequently, the influence of residual stress was accounted for using a method based on the Walker relationship (Ref 33) in conjunction with measured K_{res} (Ref 5-8, 15) to account for changes in R_{tot} as the crack size increases. These corrections to the data are described by Eq 2. To maintain a consistent approach, the same analysis procedure was applied to data from all specimens. Fig. 7(b) shows the corrected FCGR data for specimens of the AM materials and wrought specimens. When decreasing ΔK_{app} test data from specimens of the AM materials are corrected—primarily for the contributions of K_{res} —all data collapse into a single curve independent of processing method and orientation. Furthermore, the corrected AM FCGR data agree with the data for the wrought condition that have been corrected primarily for the influence of crack closure. For example, at $\Delta K = 6 \text{ MPa}\cdot\text{m}^{0.5}$, the spread in crack growth rates

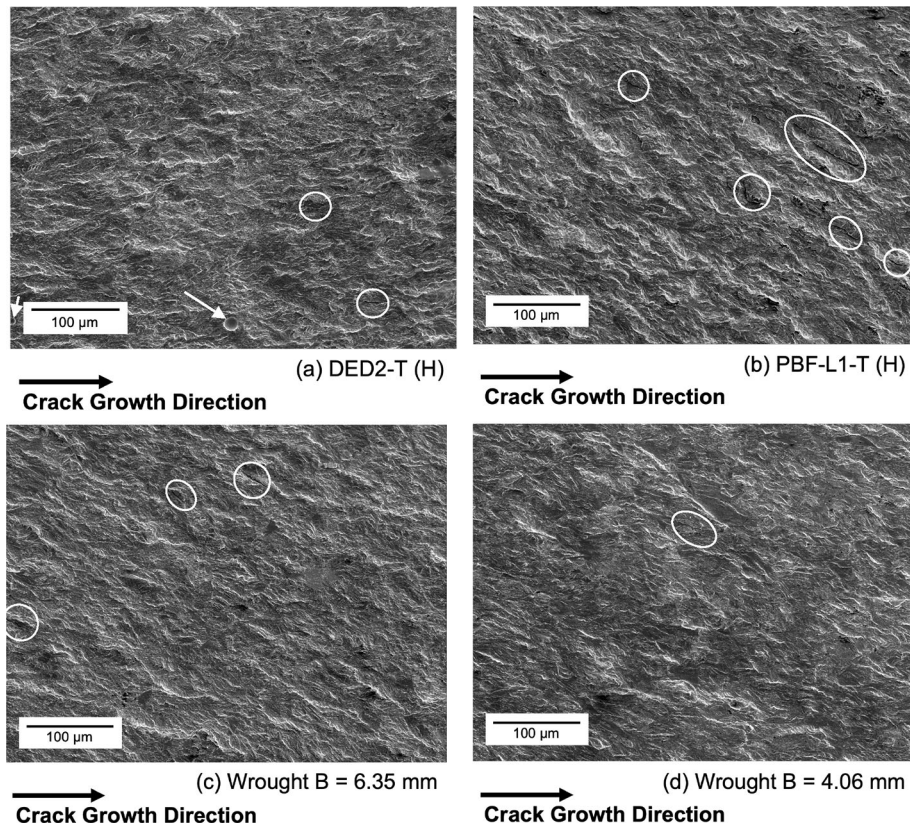


Fig 9 Fatigue crack surface images of (a) DED2-T (H) (b) PBF-L1-T (H) (c) wrought ($B = 6.35$ mm) and (d) wrought ($B = 4.06$ mm). Build direction is normal to the crack surface for the AM specimens. The arrows identify pores and the circles indicate secondary cracks.

is 4×10^{-10} to 2×10^{-9} m/cycle in the uncorrected data, but it is reduced to 6×10^{-10} to 1×10^{-9} m/cycle when the data are corrected. The agreement of the corrected data from the DED and PBF fatigue specimens with those from annealed wrought specimens highlights the significant influence of AM process-induced residual stress on fatigue crack growth behavior. The corrected data reflect the intrinsic material condition, independent of crack closure and orientation dependent residual stress fields. Additionally, it appears that any differences in crack growth rates that can be attributed to microstructure are much less significant, which is consistent with the similar, transgranular crack paths for all specimens described previously (Ref 10, 11).

After crack growth testing, specimens from decreasing ΔK_{app} tests were fractured open by rapid loading for evaluation and comparison of the fatigue surfaces. Fig. 9(a)-(d) illustrates fatigue crack surfaces of select specimens intended to be representative of material from this study. These surfaces reveal relatively smooth crack paths with similar levels of roughness in the near-threshold regime. A few pores are apparent in the DED specimen (arrows) and a small number of secondary cracks can be observed in all specimens (circles). Overall, these images from the interior of the specimens reflect relatively flat, transgranular crack paths observed in these materials. In combination with the transgranular crack profiles reported in this paper (Fig. 6) and in prior studies (Ref 10, 11), these images support the interpretation that the grain morphologies

have little impact on fatigue crack growth in this single-phase AM Type 304L stainless steel.

4. Conclusions

A comparison of additively manufactured Type 304L stainless steel produced by DED and PBF illustrates the significant influence of residual stress on FCGRs. Slitting measurements verified consistency and reproducibility in residual stress of the two AM processing methods. Tensile residual stress was larger in PBF builds compared to DED builds and this difference is attributed to higher cooling rates in PBF, which are a consequence of the fundamental differences in the processes. Measurements of FCGRs in specimens of DED and PBF materials both parallel and perpendicular to the build directions reveal differences that can be attributed to residual stress. Specifically, specimens from the PBF builds featured comparatively larger tensile residual stress intensity factors for cracks in two different orientations resulting in higher FCGR than observed in specimens of DED material. Electron backscatter diffraction images revealed similar grain shapes for both processing methods, although the grain sizes in the PBF material were smaller than in the DED. Correcting the FCGR data for the influence of the residual stress intensity factor brings the data from specimens from both processing

methods and both test orientations into agreement for this as-built austenitic single-phase Type 304L stainless steel. Furthermore, the corrected results agree with those for specimens of an annealed wrought reference material corrected for the influence of fatigue crack closure. After isolating the effects of residual stress in this way, the difference in measured yield strength does not appear to have a measurable influence on FCGRs. Additionally, transgranular crack propagation was observed in all cases (Ref 10, 11), indicating that differences in grain size and grain morphology also have relatively insignificant effects on fatigue crack growth compared to the more significant effect of residual stress.

Acknowledgments

This work was supported by a NASA Space Technology Research Fellowship (CMS) and material was provided by Sandia National Laboratories. Sandia National Laboratories is a multi-mission laboratory managed and operated by National Technology & Engineering Solutions of Sandia, LLC, a wholly owned subsidiary of Honeywell International Inc., for the U.S. Department of Energy's National Nuclear Security Administration under contract DE-NA0003525. This paper describes objective technical results and analysis. Any subjective views or opinions that might be expressed in the paper do not necessarily represent the views of the U.S. Department of Energy or the United States Government. Parts of this study were carried out at the UC Davis Center for Nano and Micro Manufacturing (CNM2). Additional material characterization in this study was carried out at the Advanced Materials Characterization and Testing facility in the Department of Materials Science and Engineering at UC Davis. The SEM images were acquired using a Thermo Fisher Quattro S ESEM funded through the NSF-MRI program DMR-1725618.

Open Access

This article is licensed under a Creative Commons Attribution 4.0 International License, which permits use, sharing, adaptation, distribution and reproduction in any medium or format, as long as you give appropriate credit to the original author(s) and the source, provide a link to the Creative Commons licence, and indicate if changes were made. The images or other third party material in this article are included in the article's Creative Commons licence, unless indicated otherwise in a credit line to the material. If material is not included in the article's Creative Commons licence and your intended use is not permitted by statutory regulation or exceeds the permitted use, you will need to obtain permission directly from the copyright holder. To view a copy of this licence, visit <http://creativecommons.org/licenses/by/4.0/>.

References

- C. Li, Z.Y. Liu, X.Y. Fang, and Y.B. Guo, Residual Stress in Metal Additive Manufacturing, *4th CIRP Conference on Surface Integrity (CSI 2018)*, (2018), **71** (*Procedia CIRP*), p 348–353
- J.J. Lewandowski and M. Seifi, Metal Additive Manufacturing: A Review of Mechanical Properties, *Annu. Rev. Mater. Res.*, 2016, **46**, p 151–186
- T. DebRoy, H.L. Wei, J.S. Zuback, T. Mukherjee, J.W. Elmer, J.O. Milewski, A.M. Beese, A. Wilson-Heid, A. De, and W. Zhang, Additive Manufacturing of Metallic Components - Process, Structure and Properties, *Prog. Mater. Sci.*, 2018, **92**, p 112–224.
- N. Shamsaei and J. Simsiriwong, Fatigue Behaviour of Additively-manufactured Metallic Parts, *Procedia Structural Integrity: 3rd International Symposium on Fatigue Design and Material Defects (FDMD 2017)*, 2017, **7**, p 3–10
- J.K. Donald and D.A. Lados, An Integrated Methodology for Separating Closure and Residual Stress Effects from Fatigue Crack Growth Rate Data, *Fatigue Fract. Eng. Mater. Struct.*, 2006, **30**(3), p 223–230
- D.A. Lados and D. Apelian, The Effect of Residual Stress on the Fatigue Crack Growth Behavior of Al-Si-Mg Cast Alloys—Mechanisms and Corrective Mathematical Models, *Metall. Mater. Trans. A Phys. Metall. Mater. Sci.*, 2006, **37A**, p 133–145
- D.A. Lados, D. Apelian, and J.K. Donald, Fracture Mechanics Analysis for Residual Stress and Crack Closure Corrections, *Int. J. Fatigue*, 2007, **29**(4), p 687–694.
- M. James, K. Maciejewski, G. Wang, D. Ball, and R. Bucci, A Methodology for Partitioning Residual Stress Effects from Fatigue Crack Growth Rate Test Data, *Mater. Perform. Charact.*, 2016, **5**(3), p 194–214.
- J.A. Newman, S.W. Smith, S. Seshadri, M.A. James, R. Brazill, R. Schultz, J.K. Donald, and A. Blair, *Characterization of Residual Stress Effects on Fatigue Crack Growth of a Friction Stir Welded Aluminum Alloy*. 2015. NASA Langley Research Center, Hampton, VA. Report No. NASA/TM-2015-218685
- C.M. Smudde, C. San Marchi, M.R. Hill, and J.C. Gibeling, Effects of Residual Stress on Orientation Dependent Fatigue Crack Growth Rates in Additively Manufactured Stainless Steel, *Int. J. Fatigue*, 2023, **169**, p 107489.
- C.M. Smudde, C.W. San Marchi, M.R. Hill, and J.C. Gibeling, Evaluation of Residual Stress Reproducibility and Orientation Dependent Fatigue Crack Growth in Powder Bed Fusion Stainless Steel, *Mater. Sci. Eng. A*, 2023, **879**, p 145266.
- Standard Specification for Chromium and Chromium-Nickel Stainless Steel Plate, Sheet, and Strip for Pressure Vessels and for General Applications*, A240/A240M-19 ASTM International, West Conshohocken, PA, (2019)
- C.M. Smudde, C.R. D'Elia, C.W. San Marchi, M.R. Hill, and J.C. Gibeling, The Influence of Residual Stress on Fatigue Crack Growth Rates of Additively Manufactured Type 304L Stainless Steel, *Int. J. Fatigue*, 2022, **162**, p 106954.
- M.R. Hill, Chapter 4: The Slitting Method, *Practical Residual Stress Measurement Methods*, G.S. Schajer Ed., Wiley, Hoboken, 2013, p 89–108
- J.A. Ronevich, C.R. D'Elia, and M.R. Hill, Fatigue Crack Growth Rates of X100 Steel Welds in High Pressure Hydrogen Gas Considering Residual Stress Effects, *Eng. Fract. Mech.*, 2018, **194**, p 42–51.
- W. Cheng and I. Finnie, *Residual Stress Measurement and the Slitting Method*, Springer, New York, 2007
- C.M. Smudde, J.C. Gibeling, and M.R. Hill, Validation of on-Line Crack Compliance Data Analysis Methods for the Residual Stress Intensity Factor, *Eng. Fract. Mech.*, 2023, **281**, 109119
- Standard Test Method for Measurement of Fatigue Crack Growth Rates*, E647-15, ASTM International, West Conshohocken, PA., (2015)
- H.J. Schindler, W. Cheng, and I. Finnie, Experimental Determination of Stress Intensity Factors Due to Residual Stresses, *Exp. Mech.*, 1997, **37**(3), p 272–277.
- D. Peckner and I.M. Bernstein, *Handbook of Stainless Steels*, McGraw-Hill Book Company, New York, 1977
- J.K. Donald, G.H. Bray, and R.W. Bush, An Evaluation of the Adjusted Compliance Ratio Technique for Determining the Effective Stress Intensity Factor, *Fatigue and Fracture Mechanics: Twenty-Ninth Volume, ASTM STP 1332*, American Society for Testing and Materials, West Conshohocken, 1999, p 674–695
- A. Charmi, R. Falkenberg, L. Ávila, G. Mohr, K. Sommer, A. Ulbricht, M. Sprengel, R. Saliwan Neumann, B. Skrotzki, and A. Evans, Mechanical Anisotropy of Additively Manufactured Stainless Steel 316L: An Experimental and Numerical Study, *Mater. Sci. Eng. A*, 2021, **799**, p 140154.
- M.L. Griffith, M.T. Ensz, J.D. Puskar, C.V. Robino, J.A. Brooks, J.A. Philliber, J.E. Smugeresky, and W.H. Hofmeister, Understanding the Microstructure and Properties of Components Fabricated by Laser Engineered Net Shaping (LENS), *Solid Freeform Add. Fabr.*, 2000, **625**, p 9–20.
- W. Hofmeister, M. Griffith, M. Ensz, and J. Smugeresky, Solidification in Direct Metal Deposition by LENS Processing, *JOM-J. Miner. Metals Mater. Soc.*, 2001, **53**(9), p 30–34.

25. B. Zheng, Y. Zhou, J.E. Smugeresky, J.M. Schoenung, and E.J. Lavernia, Thermal Behavior and Microstructural Evolution During Laser Deposition with Laser-Engineered Net Shaping: Part I Numerical Calculations, *Metall. Mater. Trans. A*, 2008, **39**(9), p 2228–2236.
26. B. Zheng, J.C. Haley, N. Yang, J. Yee, K.W. Terrassa, Y. Zhou, E.J. Lavernia, and J.M. Schoenung, On the Evolution of Microstructure and Defect Control in 316L SS Components Fabricated Via Directed Energy Deposition, *Mater. Sci. Eng. Struct. Mater. Properties Microstruct. Process.*, 2019, **764**, 138243
27. P.A. Hooper, Melt Pool Temperature and Cooling Rates in Laser Powder Bed Fusion, *Addit. Manuf.*, 2018, **22**, p 548–559.
28. L.F. Coffin, Fatigue in Machines and Structures-Power Generation, *Fatigue and Microstructure*, American Society for Metals, Metals Park, 1979, p 1–27
29. G.T. Gray, A.W. Thompson, J.C. Williams, and D.H. Stone, The Effect of Microstructure on Fatigue Crack Propagation in Pearlitic Eutectoid Steels, *Can. Metall. Q.*, 2013, **21**(1), p 73–78.
30. S. Suresh and R.O. Ritchie, A Geometric Model for Fatigue Crack Closure Induced by Fracture Surface Roughness, *Metall. Trans. A*, 1982, **13A**, p 1627–1631.
31. S. Suresh, A.K. Vasudevan, and P.E. Bretz, Mechanisms of Slow Fatigue Crack Growth in High Strength Aluminum Alloys: Role of Microstructure and Environment, *Metall. Trans. A*, 1984, **15A**, p 369–379.
32. W. Elber, Fatigue Crack Closure Under Cyclic Tension, *Eng. Fract. Mech.*, 1970, **2**, p 37–45.
33. K. Walker, The Effect of Stress Ratio During Crack Propagation and Fatigue for 2024-T3 and 7075-T6 aluminum, *Eff. Environ. Complex Load Hist. Fatigue Life*, 1970, **462**, p 1–14.

Publisher's Note Springer Nature remains neutral with regard to jurisdictional claims in published maps and institutional affiliations.